

OSRT: Omnidirectional Image Super-Resolution with Distortion-aware Transformer

Fanghua Yu^{1*} Xintao Wang^{2*} Mingdeng Cao^{2,3} Gen Li⁴ Ying Shan² Chao Dong^{1,5†}

¹SIAT, Chinese Academy of Sciences ²ARC, Tencent PCG ³The University of Tokyo

⁴Platform Technologies, Tencent Online Video ⁵Shanghai AI Lab

fanguhuayu96@gmail.com, xintaowang@tencent.com, cmd@g.ecc.u-tokyo.ac.jp

{genli, yingsshan}@tencent.com, chao.dong@siat.ac.cn

Abstract

Omnidirectional images (ODIs) have obtained lots of research interest for immersive experiences. Although ODIs require extremely high resolution to capture details of the entire scene, the resolutions of most ODIs are insufficient. Previous methods attempt to solve this issue by image super-resolution (SR) on equirectangular projection (ERP) images. However, they omit geometric properties of ERP in the degradation process, and their models can hardly generalize to real ERP images. In this paper, we propose Fisheye downsampling, which mimics the real-world imaging process and synthesizes more realistic low-resolution samples. Then we design a distortion-aware Transformer (OSRT) to modulate ERP distortions continuously and self-adaptively. Without a cumbersome process, OSRT outperforms previous methods by about 0.2dB on PSNR. Moreover, we propose a convenient data augmentation strategy, which synthesizes pseudo ERP images from plain images. This simple strategy can alleviate the over-fitting problem of large networks and significantly boost the performance of ODISR. Extensive experiments have demonstrated the state-of-the-art performance of our OSRT.

1. Introduction

In pursuit of the realistic visual experience, omnidirectional images (ODIs), also known as 360° images or panoramic images, have obtained lots of research interest in the computer vision community. In reality, we usually view ODIs with a narrow field-of-view (FOV), e.g., viewing in a headset. To capture details of the entire scene, ODIs require extremely high resolution, e.g., 4K × 8K [1]. However, due to the high industrial cost of camera sensors with high precision, the resolutions of most ODIs are insufficient.

Recently, some attempts have been made to solve this problem by image super-resolution (SR) [13, 16, 29, 40, 41].

*Equal contribution

†Corresponding author (e-mail: chao.dong@siat.ac.cn)

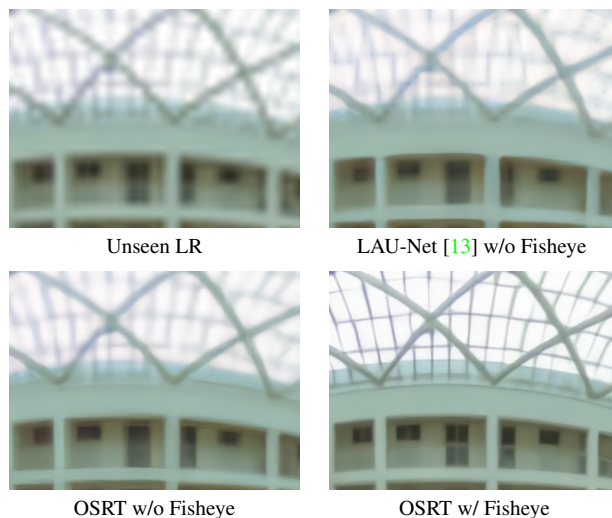


Figure 1. Visual comparisons of $\times 8$ SR results on unseen LR images¹. Fisheye denotes that the downsampling process in training stages is under Fisheye images.

As most of the ODIs are stored and transmitted in the equirectangular projection (ERP) type, the SR process is usually performed on the ERP images. To generate high-/low-resolution training pairs, existing ODISR methods [13, 16, 29, 40, 41] directly apply uniform bicubic downsampling on the original ERP images (called ERP downsampling), which is identical to general image SR settings [25, 44]. While omitting geometric properties of ERP in the degradation process, their models can hardly generalize to real ERP images. We can observe missing structures and blur textures in Fig. 1. Therefore, we need a more appropriate degradation model before studying SR algorithms. In practice, ODIs are acquired by the fisheye lens and stored in ERP. Given that the low-resolution issue in real-world scenarios is caused by insufficient sensor precision and density, the downsampling process should be applied to original-formatted images before converting into other storage types. Thus, to be conformed with real-world imaging processes, we propose to apply uniform bicubic

¹Photoed by Peter Leth on Flickr, with [CC license](#).

downsampling on Fisheye images, which are the original format of ODIs. The new downsampling process (called Fisheye downsampling) applies uniform bicubic downsampling on Fisheye images before converting them to ERP images. Our Fisheye downsampling is more conducive to exploring the geometric property of ODIs.

The key issue of ODISR algorithm design is to utilize the geometric properties of ERP images, which is also the focus of previous methods. For example, Nishiyama *et al.* [29] add a distortion-related condition as an additional input. LAU-Net [13] splits the whole ERP image into patches by latitude band and learns upscaling processes separately. However, the separated learning process will lead to information disconnection between adjacent patches. SphereSR [41] learns different upscaling functions on various projection types, but will inevitably introduce multiple-time computation costs. To push the performance upper bound, we propose the first Transformer for Omnidirectional image Super-Resolution (OSRT), and incorporate geometric properties in a distortion-aware manner. Specifically, to modulate distorted feature maps, we implement feature-level warping, in which offsets are learned from latitude conditions. In OSRT, we introduce two dedicated blocks to adapt latitude-related distortion: distortion-aware attention block (DAAB), and distortion-aware convolution block (DACB). DAAB and DACB are designed to perform distortion modulation in arbitrary Transformers and ConvNets. These two blocks can directly replace the multi-head self-attention block and convolution layer, respectively. The benefit of DAAB and DACB can be further improved when being inserted into the same backbone network. OSRT outperforms previous methods by about 0.2dB on PSNR (Tab. 2).

However, the increase of network capacity will also enlarge the overfitting problem of ODISR, which is rarely mentioned before. The largest ODIs dataset [13] contains only 1K images, which cannot provide enough diversity for training Transformers. Given that acquiring ODIs requires expensive equipment and tedious work, we propose to generate distorted ERP samples from plain images for data augmentation. In practice, we regard a plain image as a sampled perspective, and project it back to the ERP format. Then we can introduce 146K additional training patches, 6 times of the previous dataset. This simple strategy can significantly boost the performance of ODISR (Tab. 4) and alleviate the over-fitting problem of large networks (Fig. 9). A similar data augmentation method is also applied in Nishiyama *et al.* [29], but shows marginal improvement on small models under ERP downsampling settings.

Our contributions are threefold. **1)** For *problem formulation*: To generate more realistic ERP low-resolution images, we propose Fisheye downsampling, which mimics the real-world imaging process. **2)** For *method*: Combined with the geometric properties of ERP, we design a distortion-aware

Transformer, which modulates distortions continuously and self-adaptively without cumbersome process. **3)** For *data*: To reduce overfitting, we propose a convenient data augmentation strategy, which synthesizes pseudo ERP images from plain images. Extensive experiments have demonstrated the state-of-the-art performance of our OSRT.

2. Related Work

Single Image Super-Resolution (SISR). Deep learning for single image SR (SISR) is first introduced in [14]. Further works boost SR performance by CNNs [12, 15, 23, 25, 27, 30, 44], Vision Transformers (ViTs) [7, 8, 22, 24] and generative adversarial networks (GANs) [21, 36, 37, 43]. For instance, EDSR [25] removes Batch Normalization layers and applies a more complicated residual block. RCAN [44] introduces channel-wise attention mechanisms to a deeper network. SwinIR [24] proposes an image restoration Transformer based on [26]. To improve perceptual quality, adversarial training are performed as a tuning process to generate more realistic results [36, 37]. Moreover, various flexible degradation models are proposed in [36, 42] to synthesize more practical degradations.

Omnidirectional Image Super-Resolution (ODISR). Initially, ODISR models focus on the spherical assembling of LR ODIs under various projection types [2–4, 18, 28]. Recent ODISR models are performed on plane images and are fine-tuned from existing SISR models with L1 loss [16] or GAN loss [31, 45]. The improvements are limited, for they only concern the distribution gap between ODIs and plain images. Since LAU-Net [13] found pixel density in ERP ODIs is non-uniform, many studies attempt to design specific backbone networks to overcome this issue. LAU-Net [13] manually splits the whole ERP image into latitude-related patches and learns ERP distortion over different latitude ranges separately. While LAU-Net learns latitude-related ERP distortion somewhat, its non-overlapped patches lead to disconnection in whole ERP images. Nishiyama *et al.* [29] treats area stretching ratio as additional input. However, these conditions are tough to be utilized with an unmodified SISR backbone network. SphereSR [41] learns upsampling processes on various projection types (CP, ERP, Polyhedron) to mitigate the influence of non-uniformity in specific projection types. It applies a local implicit image function (LIIF) [9] to query RGB values on spherical surfaces continuously. Although SphereSR improves information consistency between various ODI projection types, they apply multiple networks to learn the upscaling process of each projection type. Given that all other projection types in SphereSR are converted from ERP, patterns under various types are reusable when distortions are properly rectified. Moreover, the complex and unstructured image data in polyhedron projection hinders further research of ODISR.

Deformable Mechanism. Dai *et al.* [31] first propose deformable convolutions to obtain information out of its regular neighborhood. Xia *et al.* [39] further verified that Vision Transformers also benefit from applying deformable mechanisms on self-attention blocks. In Video SR tasks, the deformable mechanism can be adapted to align features between adjacent frames [5, 6, 35].

3. Method

In this section, we first analyze the cause of ERP and Fisheye distortions, as well as the relationship between these two distortions (Sec. 3.1). Then, we discuss the designs of Fisheye downsampling (Sec. 3.2), distortion-aware Transformer (OSRT) (Sec. 3.3), and the convenient data augmentation strategy (Sec. 3.4).

3.1. Revisiting Distortions in ODIs

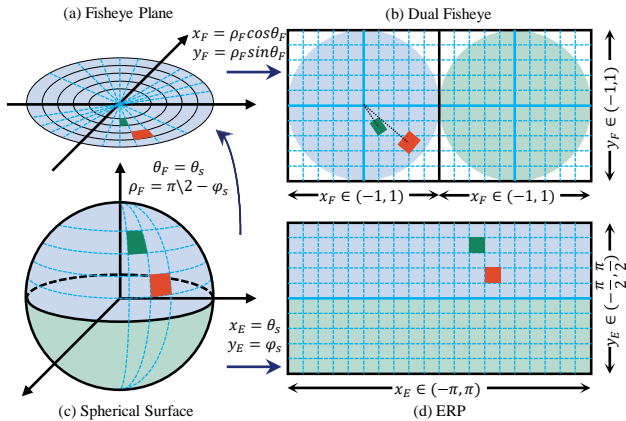


Figure 2. Geometric explanation of transforming between ERP, Fisheye, and the ideal spherical surface. To simplify, we discuss the horizontal spliced Fisheye with an aperture degree of π .

As ODIs under each projection type are constrained by different transforming equations, the distortion caused by each type is inconsistent, indicating that applying matrix operations under one projection type can introduce unexpected changes when being converted to other types. Specifically, applying uniformed bicubic downsampling on ERP images will affect the distribution of pixel density on Fisheye images, which are the original-formatted image type of imaging process in real-world scenarios. To analyze the specific effect of ERP downsampling on the Fisheye image, we revisit the cause of distortions in ERP and Fisheye.

As we assume that viewing directions are uniformly distributed, the data points in an ideal ODI should be uniformly distributed on a spherical surface. In practice, there is a trade-off between the uniformity of the spherical surface and the structural degree. ERP is the most convenient projection type for storage or transmission, but it is also the projection type that suffers the heaviest distortion. To better explain the causation of distortions, we follow the definition

of stretching ratio (\mathbf{K}) in [32], which represents distortion degree at different locations from the target projection type to the ideal spherical surface. \mathbf{K} is determined by area variation from one projection type to another. When the target type is uniforming spherical surface, \mathbf{K} is defined as:

$$\mathbf{K}(x, y) = \frac{\delta S(\theta, \varphi)}{\delta P(x, y)} = \frac{\cos(\varphi)|d\theta d\varphi|}{|dxdy|} = \frac{\cos(\varphi)}{|J(\theta, \varphi)|}, \quad (1)$$

where $\delta S(\cdot, \cdot)$ and $\delta P(\cdot, \cdot)$ represent the area on the spherical surface and the projection plane, respectively. $|didj|$ represents plane microunit. $|J(\theta, \varphi)|$ is the Jacobian determinant from spherical coordinate to projection coordinate.

ERP distortion. The coordinate in ERP is defined as $x = \theta$ and $y = \varphi$. ERP stretching ratio can be derived as:

$$\mathbf{K}_{\text{ERP}}(x, y) = \cos(\varphi) = \cos(y), \quad (2)$$

where $x \in (-\pi, \pi)$, $y \in (-\frac{\pi}{2}, \frac{\pi}{2})$.

From Eq. (2), we conclude that ERP distortion is only determined by its latitude degree. \mathbf{K}_{ERP} is reduced to zero when the absolute value of latitude degree increases to $\pi/2$, which represents that pixel density on the polar areas of ERP images is closer to zero. As shown in Fig. 2 (c), with the increasing of the absolutely value of latitude degree ($|\varphi_s|$), the corresponding area on the spherical surface of an ERP microunit is gradually decreased to zero. In conclusion, ERP distortion is caused by variable stretching ratios \mathbf{K}_{ERP} , and is the heaviest in the polar areas.

Fisheye distortion. The coordinate in Fisheye can be derived from $\theta = \arctan(\frac{y}{x})$ and $\varphi = (1 - \sqrt{x^2 + y^2}) \times \frac{\pi}{2}$. The stretching ratios of Fisheye can be derived as²:

$$\mathbf{K}_{\text{Fisheye}}(x, y) = \frac{\frac{\pi}{2} \sin(\frac{\pi}{2} \sqrt{x^2 + y^2})}{\sqrt{x^2 + y^2}}, \quad (3)$$

where $\sqrt{x^2 + y^2} \in (0, 1)$.

$\mathbf{K}_{\text{Fisheye}}$ is determined by distance from the fisheye center. As $(\mathbf{K}_{\text{Fisheye}})^{-1}$ is bounded, fisheye projection is closer to uniform distribution than ERP. Moreover, it introduces much slighter distortion at the polar.

Relationship between ERP and Fisheye distortions.

To simplify, here we only discuss a typical Fisheye with an aperture degree of π and a horizontal slicing plane³. In this case, the ERP coordinates and Fisheye's polar coordinates correspond linearly. We can quantize the relationship by:

$$\mathbf{K}_{\text{ERP|Fisheye}}(\theta, \varphi) = \frac{\mathbf{K}_{\text{ERP}}(x_E, y_E)}{\mathbf{K}_{\text{Fisheye}}(x_F, y_F)} = \frac{\pi}{2} - |\varphi|, \quad (4)$$

where θ, φ are spherical coordinates on the sphere, x_E, y_E (x_F, y_F) denotes the plain coordinate under ERP (Fisheye).

²Detailed derivative processes can be found in the supplementary file.

³The influence of Fisheye formats with arbitrary splicing plane is discussed in the supplementary file.

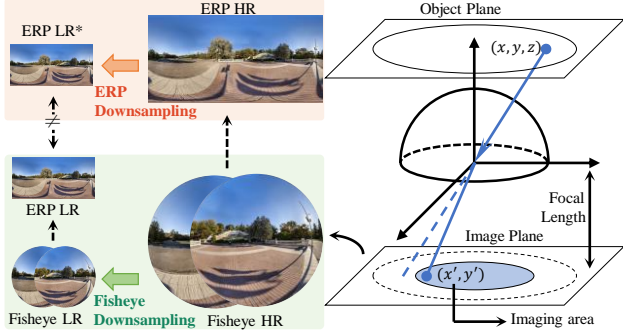


Figure 3. Downsampling process of ODIs (left) and imaging process in real world (right). * denotes that LR images synthesized from different downsampling processes are inconsistent.

From Eqs. (2) to (4), we conclude that when uniformed downsampling is performed on ERP, the kernel size of equivalent Fisheye downsampling is non-uniformed. Especially when fisheye projection is spliced horizontally, the kernel size is proportional with $\pi/2 - |\varphi|$.

3.2. Learning with More Realistic Degradation

As depicted in Fig. 3, the original-formatted projection type in ODI acquiring process is fisheye projection. Given that real-world low-resolution issues are caused by insufficient precision and density of sensors, we consider that the degeneration process should be directly applied to original-formatted images before the type conversion.

Ideally, as camera sensors are arranged in uniform arrays, pixel density on original-formatted images is consistent everywhere. Thus, for a realistic ODI, the pixel density on Fisheye should be a constant. As discussed in Sec. 3.1, applying uniformed downsampling on ERP means applying downsampling of variable kernel size on Fisheye. The variable kernel size leads to variable Fisheye pixel density, which results in unrealistic LR images. In conclusion, the ERP downsampling in previous methods influences the intrinsic distribution of pixel density in original-formatted images, which leads to unrealistic ODIs. When the downsampling process happens on Fisheye, the Fisheye pixel density is unchanged, which fits the real-world imaging process and synthesizes more realistic LR pairs.

Process of Fisheye downsampling. To generate more realistic LR ODIs, we mimic the real-world imaging process and apply bicubic downsampling on Fisheye images. One single Fisheye image can only store information about a hemisphere. Hence, ERP images are converted to dual Fisheye images. Before downsampling, Fisheye images are padded by a FOV larger than 180° to avoid edge disconnections. This padding operation will not influence the geometric transforming relation between ERP and Fisheye. As Fisheye data is unstructured and Fisheye distortion is more complicated than ERP distortion, we still learn the upscaling process under ERP. Thus we reconvert LR images to the

ERP format. The overall process of Fisheye downsampling are described in Fig. 3.

3.3. OSRT: Modulate Distortion in ODIs

Overall. As discussed in Sec. 3.1, ERP images suffer a distortion caused by a non-consistency area stretching ratio from an ideal spherical surface. Referred from Eq. (2), for an LR input $X_i \in \mathbb{R}^{C \times M \times N}$, the distortion map $C_d \in \mathbb{R}^{1 \times M \times N}$ is derived by:

$$C_d = \cos\left(\frac{m + 0.5 - M/2}{M}\pi\right), \quad (5)$$

where m is the current height of LR input.

Previous methods tend to treat C_d as an additional input of X_i [29], or re-weighting parameters by C_d [19]. Although these solutions can benefit from building awareness of distortion, continuous and amorphous distortions cannot be adequately fitted by scattering and structured convolution operations. While previous methods cannot fully explore the advantage of C_d , we intend to design a novel block for learning distorted patterns continuously. In VSR tasks, the deformable mechanism is proposed to align features between adjacent frames [33, 35]. Unlike standard DCN [11], which calculates offsets from the input feature map, offsets are calculated from bi-directional optical flow in VSR pipelines. Inspired by feature-level flow warping in VSR, we find that the deformable mechanism is a feasible solution for continuous mappings. Consequently, we modulate ERP distortion by feature-level warping operations. As shown in Fig. 4, C_d is only utilized to calculate the deformable offsets Δp . To keep compatibility with arbitrary ConvNets and Transformers, we propose two blocks to modulate ERP distortion, which can directly replace the multi-head self-attention blocks in Transformers and the standard convolution layers in ConvNets, respectively.

Distortion-aware attention block (DAAB). As depicted in Fig. 4 (a), a distortion condition guided deformable self-attention is proposed to learn correlations between the distorted input F_{i-1} and its corresponding modulated feature map \tilde{F}_{i-1} . DAAB is formulated as:

$$\Delta p_i = H_{\text{offset}_i}(C_d, C_w), \tilde{F}_{i-1} = \phi(F_{i-1}; p_i + \Delta p_i), \quad (6)$$

$$F_i = H_{\text{SA}}(F_{i-1}W_{q_i}, \tilde{F}_{i-1}W_{k_i}, \tilde{F}_{i-1}W_{v_i}), \quad (7)$$

where $H_{\text{offset}_i}(\cdot)$ denotes the i -th convolution block to calculate offset maps $\Delta p_i \in \mathbb{R}^{2 \times H \times W}$, and H_{SA} denotes standard self-attention formula. $H_{\text{offset}}(\cdot)$ consists of 1×1 convolution block with two hidden layers. The input of $H_{\text{offset}}(\cdot)$ is concatenated by the latitude-related distortion condition $C_d \in \mathbb{R}^{1 \times H \times W}$ and the window condition $C_w \in \mathbb{R}^{2 \times H \times W}$. C_w is a linear position encoding within a self-attention kernel. $\phi(\cdot, \cdot)$ denotes a bilinear interpolation, and $W_{q_i}, W_{k_i}, W_{v_i}$ denote i -th weight matrix of query, key, and

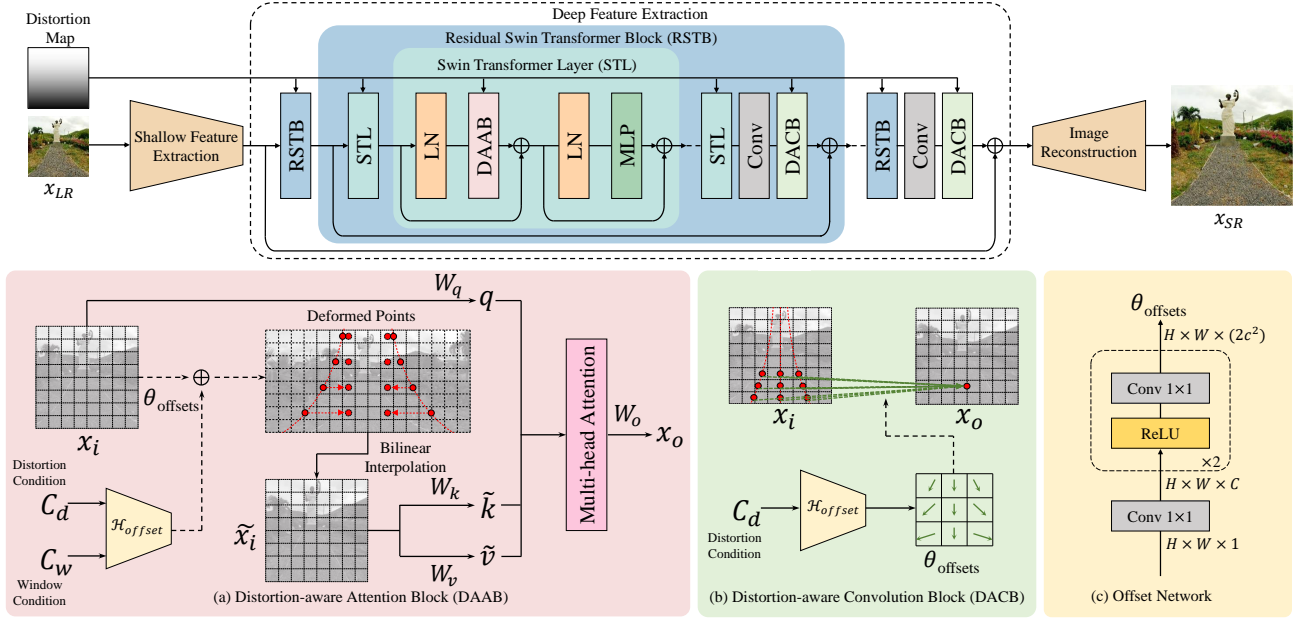


Figure 4. Overall illustration of OSRT. From SwinIR [24], we replace the standard multi-head self-attention block with DAAB and insert DACB behind the end of the RSTB. Channel dimensions of θ_{offsets} in DAAB and DACB are 2 and 18, respectively.

value, respectively. For multi-head self-attention blocks, $H_{\text{offset}_i}(\cdot)$ is identical in calculations of parallel heads.

Distortion-aware convolution block (DACB). As shown in Fig. 4 (b), we apply a standard deformable convolution layer with a substituted input for offset calculation. Modulated output F_i is extracted as:

$$\Delta p_i = H_{\text{offset}_i}(C_d), F_i = H_{\text{DCN}_i}(F_{i-1}, \Delta p_i), \quad (8)$$

where $H_{\text{DCN}}(F, \Delta p)$ denotes standard deformable convolution layer in [47]. The architecture of $H_{\text{offset}_i}(\cdot)$ is identical to that in DAAB. As the kernel size of DCN is 3×3 in DACB, the output channel dimension of offsets maps is 18.

OSRT. In practice, we propose an Omnidirectional image Super-Resolution Transformer, named OSRT. SwinIR [24] is selected as the basic architecture for its strong reconstruction ability in the SISR task. To learn distortion rectified representations, we stack a DACB after the last convolution layer of each residual swin Transformer block and replace all self-attention blocks as DAAB. The feature dimension of OSRT is reduced from 180 to 156 to maintain identical parameters with SwinIR.

3.4. Boosting ODISR Performance by Plain Images

As the capacity of OSRT is relatively large, it suffers overfitting for large upscaling factors (Fig. 9). Given that acquiring ODIs are expensive, we propose to generate pseudo ERP images from 2D plain images to tackle this issue. After being sampled by sliding windows, the patch of plain images is treated as a plain perspective. By converting from Perspective to ERP, plain images are distorted in the same way as ERP. Considering that distortion of a Perspective is enlarged by its FOV degree, a relatively small FOV

degree of 90° is applied. For a given pseudo Perspective, θ_p is fixed at 0 and φ_p is derived by:

$$\Phi_p = \varphi_h + z_0, \quad (9)$$

where φ_h is determined by patch locations and z_0 is orderly sampled from $\{-15^\circ, 0^\circ, 15^\circ\}$.

To maximize the approximate data distribution of ODIs, we horizontally split a plain image into three sub-images and define φ_h as $-30^\circ, 0^\circ, 30^\circ$ respectively. Pseudo ERP images are cropped to remove the black border. As shown in Fig. 5, we get a new ERP dataset (called DF2K-ERP) by implementing the augmentation pipeline on widely-used plain image dataset DF2K [25, 34]. The DF2K-ERP dataset consists of 146K high-quality ERP image patches with a patch size larger than 256.

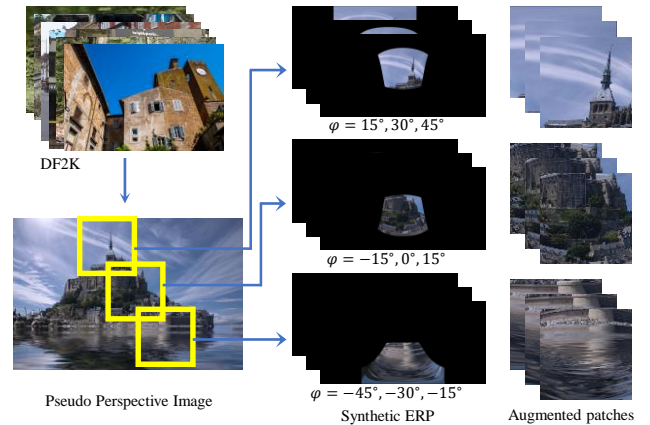


Figure 5. Synthetic process of DF2K-ERP.

Method	Scale	ODI-SR				SUN 360 Panorama			
		PSNR	SSIM	WS-PSNR	WS-SSIM	PSNR	SSIM	WS-PSNR	WS-SSIM
Bicubic	×2	28.21	0.8215	27.61	0.8156	28.14	0.8118	28.01	0.8321
RCAN [44]		30.08	0.8723	29.49	0.8714	30.56	0.8712	31.18	0.8969
SRResNet [37]		30.16	0.8717	29.59	0.8697	30.65	0.8714	31.20	0.8953
EDSR [25]		30.32	0.8770	29.68	0.8727	30.89	0.8784	31.42	0.8995
SwinIR [24]		30.52	0.8819	29.87	0.8772	31.21	0.8852	31.78	0.9051
SwinIR [†] [24]		30.64	0.8821	30.00	0.8777	31.33	0.8855	31.98	0.9059
OSRT [†]		30.77	0.8846	30.11	0.8795	31.52	0.8888	32.14	0.9081
Bicubic	×4	25.59	0.7118	24.95	0.6923	25.29	0.6993	24.90	0.7083
RCAN [44]		26.85	0.7621	26.15	0.7485	27.10	0.7660	26.99	0.7856
SRResNet [37]		26.91	0.7597	26.24	0.7457	27.10	0.7618	26.99	0.7812
EDSR [25]		26.97	0.7589	26.30	0.7458	27.19	0.7633	27.10	0.7827
SwinIR [24]		27.12	0.7663	26.44	0.7523	27.39	0.7707	27.30	0.7901
SwinIR [†] [24]		27.31	0.7735	26.61	0.7589	27.71	0.7804	27.64	0.7996
OSRT [†]		27.41	0.7762	26.70	0.7609	27.84	0.7835	27.77	0.8020

Table 1. SR results under Fisheye downsampling. † denotes applying DF2K-ERP as augmented dataset. Best results are shown in **Bold**.

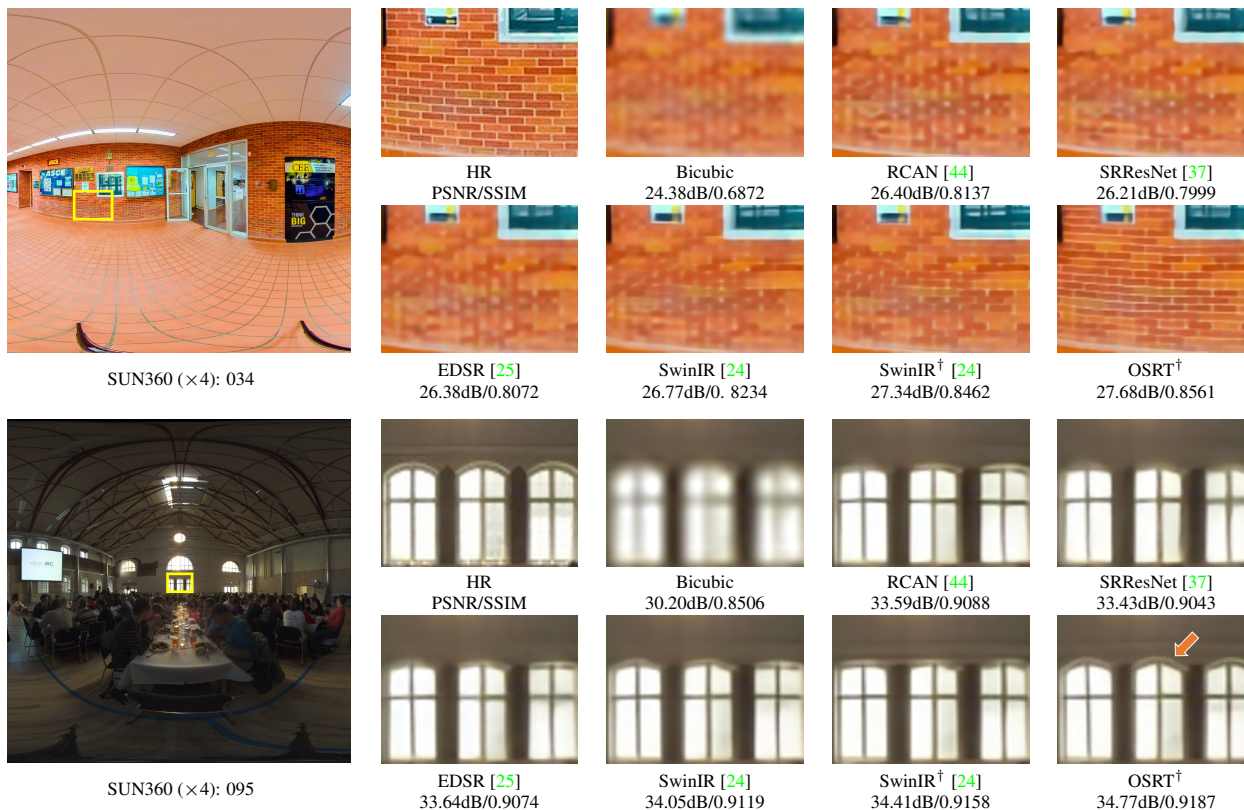


Figure 6. Visual comparisons of ×4 SR results under Fisheye downsampling.

4. Experiments

4.1. Experimental Setup

ODI-SR dataset [13] and SUN360 Panorama dataset [40] are used in our experiment. In the training phase, we follow the data split setting in [13] and train on the ODI-SR training set. The resolution of the ERP HR is 1024×2048 , and the upscaling factors are ×2 and ×4. Fisheye downsampling is applied as our pre-defined downsampling kernel. Loss is calculated by L1 distance and optimized by Adam [20], with an initial learning rate of 2×10^{-4} , a total batch size of 32, and an input patch size of 64. We

train OSRT for 500k iterations and halve the learning rate at 250k, 400k, 450k and 475k. In evaluation, we test on the ODI-SR testing set and SUN360 dataset. PSNR [17], SSIM [38], and their distortion re-weighted versions (WS-PSNR [32], WS-SSIM [46]) are used as evaluation metrics.

4.2. Evaluation under Fisheye Downsampling

When the downsampling process is performed on Fisheye images, we train SRResNet [37], EDSR [25], RCAN [44], and SwinIR [24] for comparison.

Quantitative results. As shown in Tab. 1, with the help of additional DF2K-ERP training patches, OSRT out-

Method	$\times 8$				$\times 16$			
	ODI-SR		SUN 360 Panorama		ODI-SR		SUN 360 Panorama	
	WS-PSNR	WS-SSIM	WS-PSNR	WS-SSIM	WS-PSNR	WS-SSIM	WS-PSNR	WS-SSIM
Bicubic	19.64	0.5908	19.72	0.5403	17.12	0.4332	17.56	0.4638
SRCNN [14]	20.08	0.6112	19.46	0.5701	18.08	0.4501	17.95	0.4684
EDSR [25]	23.97	0.6417	22.46	0.6341	21.12	0.5698	21.06	0.5645
RCAN [44]	24.26	0.6628	23.88	0.6542	21.94	0.5824	21.74	0.5742
360-SS [31]	21.65	0.6417	21.48	0.6352	19.65	0.5431	19.62	0.5308
LAU-Net [13]	24.36	0.6801	24.02	0.6708	22.07	0.5901	21.82	0.5824
SphereSR [41]	24.37	0.6777	24.17	0.6820	22.51	0.6370	21.95	0.6342
OSRT	24.53	0.6780	24.38	0.7072	22.69	0.6261	22.13	0.6388

Table 2. SR results under ERP downsampling.

performs previous methods by 0.3dB on PSNR. Although directly applying SwinIR on the ODISR task has already reached SOTA performance, OSRT surpasses SwinIR over 0.1dB on two datasets for both $\times 2$ and $\times 4$ SR tasks, which demonstrates the effectiveness of its distortion modulation ability. The performance of RCAN degrades under Fisheye downsampling, which is caused by the incompatibility between channel attention and Fisheye downsampling⁴.

Qualitative comparison. Fig. 6 shows the visualization results of $\times 4$ ODISR task. While other methods struggle to understand the geometric transformation process in distorted images, OSRT can reconstruct sharp and accurate boundaries with the advantages of distortion modulation. It is observed that OSRT is skilled at reconstructing rigid texture. Moreover, benefiting from the distortion modulation ability, OSRT can preserve the original structure as most when being projected to other projection types (Fig. 7).

4.3. Evaluation under ERP Downsampling

To compare with previous ODISR methods [13, 31, 41], we train OSRT under the previous ERP setting. Regardless of over-fitting issues, we only train on the dataset provided by [13] for fairness. As shown in Tab. 2, OSRT still outperforms LAU-Net [13] and SphereSR [41] under large upscaling factor and ERP downsampling. Without a complicated training pipeline and discrete inference process, OSRT yields the best PSNR values and surpasses all previous methods on most SSIM-related metrics (three of four).

4.4. Ablation Study and Discussion

In this section, we prove the effectiveness of Fisheye downsampling, OSRT components, and augmented DF2K-ERP. We then explain the distortion modulation ability of OSRT by visualizing offsets in deformable blocks.

Fisheye downsampling. As shown in Fig. 1, the SR model trained under ERP downsampling is more likely to generate blur details and missing structures in real-world scenarios. These artifacts cannot be removed by a superior backbone network, but can be eliminated by a more realistic imaging process. More importantly, ERP downsampling directly covers the geometric property of ERP images

feature dim	DACB	DAAB	ODI-SR		SUN360		Params. (M)
			PSNR	SSIM	PSNR	SSIM	
60	\times	\times	30.27	0.8739	30.78	0.8742	0.91
60	\checkmark	\times	30.41	0.8775	31.00	0.8793	1.16
60	\times	w/o C_w	30.31	0.8746	30.83	0.8755	1.00
60	\times	w/ C_w	30.32	0.8746	30.84	0.8753	1.01
60	\checkmark	w/ C_w	30.44	0.8780	31.04	0.8800	1.26
72	\times	\times	30.32	0.8748	30.85	0.8755	1.29

Table 3. Ablation study on OSRT components. All models are trained on $\times 2$ SR task under Fisheye downsampling.

and makes the ODISR task identical to the standard plain image super-resolution task. The evidence is that a standard SISR model (SwinIR) trained on a plain image dataset (DF2K) can outperform previous SOTA in the ODISR task, which yields WS-PSNR results of 24.63dB/24.49dB (22.68dB/22.13dB) on $\times 8$ ($\times 16$) ODI-SR/SUN360 testing set, respectively. In conclusion, when the intrinsic property of ODIs is broken by ERP downsampling, the ODISR task degenerates into a plain image super-resolution task with a particular data distribution.

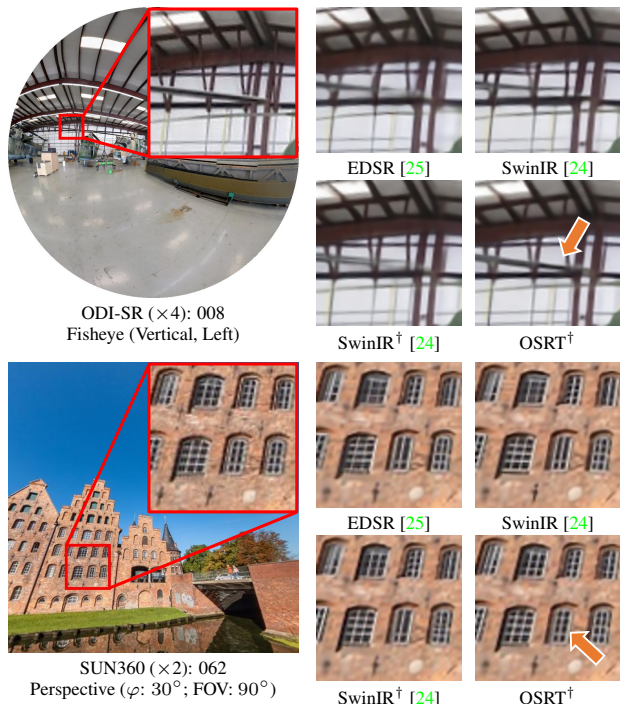


Figure 7. Visual comparisons for SR of Fisheye and Perspective images. † denotes applying DF2K-ERP as augmented dataset.

⁴The cause is discussed in the supplementary file.

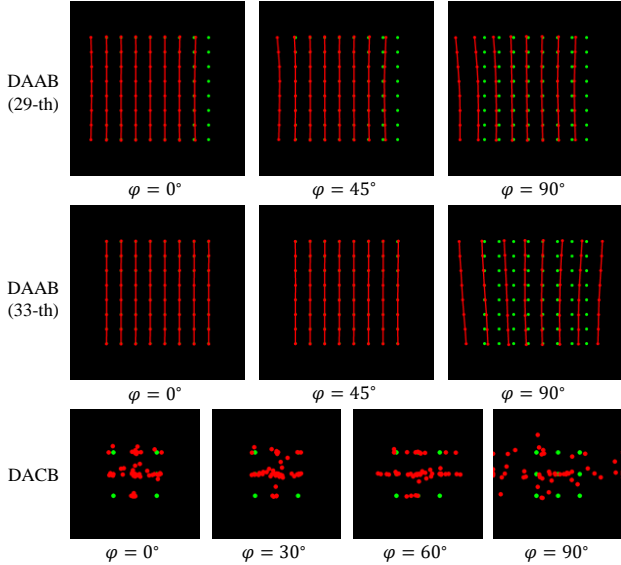


Figure 8. Visualizations of offset maps in OSRT. Reference and deformed points are depicted in green and red, respectively. The deformable kernel is sparse in the polar area.

OSRT components. To study the effectiveness of each component in OSRT, we propose a light version of OSRT (OSRT-light) for ablation study, which corresponds with the official SwinIR-light [24]. As proofed in Tab. 3, all components in OSRT are beneficial for modulating ERP distortion. The advantages of DACB and DAAB can be stacked when being applied in the same network. Compared with simply expanding the feature dimension of SwinIR to match the network complexity, the overall improvements of OSRT is more significant (+0.05dB vs. +0.2dB).

Offsets in OSRT. To investigate whether the deformable mechanism in OSRT can modulate distortion as expected, we visualize offsets map in a well-trained OSRT. As depicted in Fig. 8, deformable kernels in both DAAB and DACB tend to gather at the equator and scatter at the po-

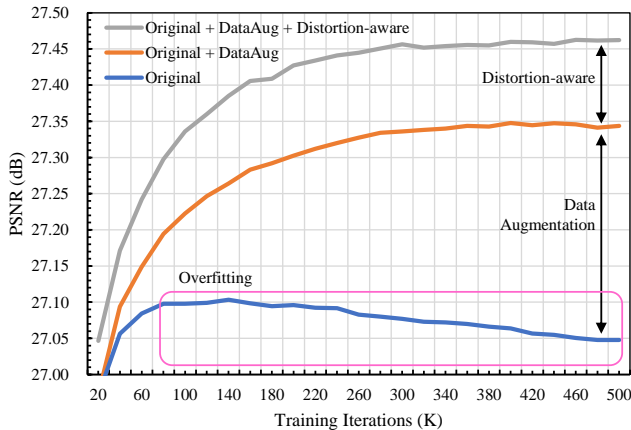


Figure 9. Training process of Transformers on $\times 4$ ODISR task. The overfitting issue is tackled by our augmentation scheme.

Backbone network	Datasets	Training scheme	Scale	SUN360	
				PSNR	SSIM
SwinIR	ODI-SR	N/A		31.21	0.8852
SwinIR	DF2K/ODI-SR	one-stage	$\times 2$	31.26	0.8841
SwinIR	DF2K-ERP/ODI-SR	one-stage		31.33	0.8855
SwinIR	DF2K-ERP/ODI-SR	two-stage		31.17	0.8818
OSRT	DF2K-ERP/ODI-SR	one-stage		31.52	0.8888
SwinIR	ODI-SR	N/A		27.39	0.7707
SwinIR	DF2K/ODI-SR	one-stage	$\times 4$	27.59	0.7768
SwinIR	DF2K-ERP/ODI-SR	one-stage		27.71	0.7804
SwinIR	DF2K-ERP/ODI-SR	two-stage		27.74	0.7795
OSRT	DF2K-ERP/ODI-SR	one-stage		27.84	0.7835

Table 4. Ablation study on data augmentation. The results of ODI-SR (In the supplementary file) are in the same trend as SUN360.

lar, which conforms to the geometric distribution of pixel density in ERP images. Besides, DAAB can also learn an overall kernel translation (the 29th DAAB), which can be regarded as a self-adaptively shift window operation.

Pseudo ERP patches. In Sec. 3.4, we propose a distorted dataset DF2K-ERP to tackle over-fitting issues. We train a standard SwinIR on diverse datasets and training schemes to study the influence of data augmentation separately. As shown in Tab. 4, while training on ODI-SR and DF2K, distortion operations in DF2K lead to better performance. Compared with fine-tuning on DF2K-ERP pre-trained models (two-stage), training on two datasets jointly (one-stage) shows better results. We infer that there is a domain gap between ODI-SR and DF2K-ERP, which is caused by omitted Perspective distortion⁵. Moreover, the advantage of distortion modulation mechanisms in OSRT is enlarged when additional training patches are applied. Fig. 9 proves that our data augmentation scheme overcomes the over-fitting issue and improves the reconstruction ability.

5. Conclusion

In this paper, we find that the previous downsampling process in the ODISR task harms the intrinsic distribution of pixel density in ODIs, which leads to poor generalization ability in real-world scenarios. To tackle this issue, we propose Fisheye downsampling, which mimics the real-world imaging process to preserve the realistic density distribution. After refining the downsampling process, we design a distortion-aware Transformer (OSRT) to modulate distortions continuously and self-adaptively. OSRT learns offsets from the distortion-related condition and rectifies distortion by feature-level warping. Moreover, to alleviate the over-fitting problem of large networks, we propose to synthesize additional ERP training data from the plain images. Extensive experiments have demonstrated the state-of-the-art performance of our OSRT.

Limitation. This work focuses on the feature extract process in ODISR. However, to get a better viewing experience, the process of sampling ERP images into viewing types also requires careful design.

⁵Detailed analysis can be found in the supplementary file.

References

- [1] Hao Ai, Zidong Cao, Jinjing Zhu, Haotian Bai, Yucheng Chen, and Ling Wang. Deep learning for omnidirectional vision: A survey and new perspectives. *arXiv preprint arXiv:2205.10468*, 2022. **1**
- [2] Zafer Arican and Pascal Frossard. L1 regularized super-resolution from unregistered omnidirectional images. In *2009 IEEE International Conference on Acoustics, Speech and Signal Processing*, pages 829–832. IEEE, 2009. **2**
- [3] Zafer Arican and Pascal Frossard. Joint registration and super-resolution with omnidirectional images. *IEEE Transactions on Image Processing*, 20(11):3151–3162, 2011. **2**
- [4] Luigi Bagnato, Yannick Boursier, Pascal Frossard, and Pierre Vanderghyest. Plenoptic based super-resolution for omnidirectional image sequences. In *2010 IEEE International Conference on Image Processing*, pages 2829–2832. IEEE, 2010. **2**
- [5] Kelvin CK Chan, Xintao Wang, Ke Yu, Chao Dong, and Chen Change Loy. Basicvsr: The search for essential components in video super-resolution and beyond. In *Proceedings of the IEEE/CVF Conference on Computer Vision and Pattern Recognition*, pages 4947–4956, 2021. **3**
- [6] Kelvin CK Chan, Shangchen Zhou, Xiangyu Xu, and Chen Change Loy. Basicvsr++: Improving video super-resolution with enhanced propagation and alignment. In *Proceedings of the IEEE/CVF Conference on Computer Vision and Pattern Recognition*, pages 5972–5981, 2022. **3**
- [7] Hanting Chen, Yunhe Wang, Tianyu Guo, Chang Xu, Yiping Deng, Zhenhua Liu, Siwei Ma, Chunjing Xu, Chao Xu, and Wen Gao. Pre-trained image processing transformer. In *Proceedings of the IEEE/CVF Conference on Computer Vision and Pattern Recognition*, pages 12299–12310, 2021. **2**
- [8] Xiangyu Chen, Xintao Wang, Jiantao Zhou, and Chao Dong. Activating more pixels in image super-resolution transformer. *arXiv preprint arXiv:2205.04437*, 2022. **2**
- [9] Yinbo Chen, Sifei Liu, and Xiaolong Wang. Learning continuous image representation with local implicit image function. In *Proceedings of the IEEE/CVF conference on computer vision and pattern recognition*, pages 8628–8638, 2021. **2**
- [10] Xiaojie Chu, Liangyu Chen, Chengpeng Chen, and Xin Lu. Improving image restoration by revisiting global information aggregation. In *European Conference on Computer Vision*, pages 53–71. Springer, 2022. **12, 13**
- [11] Jifeng Dai, Haozhi Qi, Yuwen Xiong, Yi Li, Guodong Zhang, Han Hu, and Yichen Wei. Deformable convolutional networks. In *Proceedings of the IEEE international conference on computer vision*, pages 764–773, 2017. **4**
- [12] Tao Dai, Jianrui Cai, Yongbing Zhang, Shu-Tao Xia, and Lei Zhang. Second-order attention network for single image super-resolution. In *Proceedings of the IEEE/CVF conference on computer vision and pattern recognition*, pages 11065–11074, 2019. **2**
- [13] Xin Deng, Hao Wang, Mai Xu, Yichen Guo, Yuhang Song, and Li Yang. Lau-net: Latitude adaptive upscaling network for omnidirectional image super-resolution. In *Proceedings of the IEEE/CVF Conference on Computer Vision and Pattern Recognition*, pages 9189–9198, 2021. **1, 2, 6, 7, 12**
- [14] Chao Dong, Chen Change Loy, Kaiming He, and Xiaoou Tang. Image super-resolution using deep convolutional networks. *IEEE transactions on pattern analysis and machine intelligence*, 38(2):295–307, 2015. **2, 7**
- [15] Chao Dong, Chen Change Loy, and Xiaoou Tang. Accelerating the super-resolution convolutional neural network. In *European conference on computer vision*, pages 391–407. Springer, 2016. **2**
- [16] Vida Fakour-Sevom, Esin Guldogan, and Joni-Kristian Kämäräinen. 360 panorama super-resolution using deep convolutional networks. In *Int. Conf. on Computer Vision Theory and Applications (VISAPP)*, volume 1, 2018. **1, 2**
- [17] Quan Huynh-Thu and Mohammed Ghanbari. Scope of validity of psnr in image/video quality assessment. *Electronics letters*, 44(13):800–801, 2008. **6**
- [18] Hiroshi Kawasaki, Katsushi Ikeuchi, and Masao Sakauchi. Super-resolution omnidirectional camera images using spatio-temporal analysis. *Electronics and Communications in Japan (Part III: Fundamental Electronic Science)*, 89(6):47–59, 2006. **2**
- [19] Renata Khasanova and Pascal Frossard. Geometry aware convolutional filters for omnidirectional images representation. In *International Conference on Machine Learning*, pages 3351–3359. PMLR, 2019. **4**
- [20] Diederik P Kingma and Jimmy Ba. Adam: A method for stochastic optimization. *arXiv preprint arXiv:1412.6980*, 2014. **6**
- [21] Christian Ledig, Lucas Theis, Ferenc Huszár, Jose Caballero, Andrew Cunningham, Alejandro Acosta, Andrew Aitken, Alykhan Tejani, Johannes Totz, Zehan Wang, et al. Photo-realistic single image super-resolution using a generative adversarial network. In *Proceedings of the IEEE conference on computer vision and pattern recognition*, pages 4681–4690, 2017. **2**
- [22] Wenbo Li, Xin Lu, Jiangbo Lu, Xiangyu Zhang, and Jiaya Jia. On efficient transformer and image pre-training for low-level vision. *arXiv preprint arXiv:2112.10175*, 2021. **2**
- [23] Zheyuan Li, Yingqi Liu, Xiangyu Chen, Haoming Cai, Jinjin Gu, Yu Qiao, and Chao Dong. Blueprint separable residual network for efficient image super-resolution. In *Proceedings of the IEEE/CVF Conference on Computer Vision and Pattern Recognition*, pages 833–843, 2022. **2**
- [24] Jingyun Liang, Jie Zhang Cao, Guolei Sun, Kai Zhang, Luc Van Gool, and Radu Timofte. Swinir: Image restoration using swin transformer. In *Proceedings of the IEEE/CVF International Conference on Computer Vision*, pages 1833–1844, 2021. **2, 5, 6, 7, 8, 14**
- [25] Bee Lim, Sanghyun Son, Heewon Kim, Seungjun Nah, and Kyoung Mu Lee. Enhanced deep residual networks for single image super-resolution. In *Proceedings of the IEEE conference on computer vision and pattern recognition workshops*, pages 136–144, 2017. **1, 2, 5, 6, 7, 14**
- [26] Ze Liu, Yutong Lin, Yue Cao, Han Hu, Yixuan Wei, Zheng Zhang, Stephen Lin, and Baining Guo. Swin transformer: Hierarchical vision transformer using shifted windows. In

- Proceedings of the IEEE/CVF International Conference on Computer Vision*, pages 10012–10022, 2021. [2](#)
- [27] Yiqun Mei, Yuchen Fan, and Yuqian Zhou. Image super-resolution with non-local sparse attention. In *Proceedings of the IEEE/CVF Conference on Computer Vision and Pattern Recognition*, pages 3517–3526, 2021. [2](#)
- [28] Hajime Nagahara, Yasushi Yagi, and Masahiko Yachida. Super-resolution from an omnidirectional image sequence. In *2000 26th Annual Conference of the IEEE Industrial Electronics Society. IECON 2000. 2000 IEEE International Conference on Industrial Electronics, Control and Instrumentation. 21st Century Technologies*, volume 4, pages 2559–2564. IEEE, 2000. [2](#)
- [29] Akito Nishiyama, Satoshi Ikehata, and Kiyoharu Aizawa. 360 single image super resolution via distortion-aware network and distorted perspective images. In *2021 IEEE International Conference on Image Processing (ICIP)*, pages 1829–1833. IEEE, 2021. [1](#), [2](#), [4](#)
- [30] Ben Niu, Weilei Wen, Wenqi Ren, Xiangde Zhang, Lianping Yang, Shuzhen Wang, Kaihao Zhang, Xiaochun Cao, and Haifeng Shen. Single image super-resolution via a holistic attention network. In *European conference on computer vision*, pages 191–207. Springer, 2020. [2](#)
- [31] Cagri Ozcinar, Aakanksha Rana, and Aljosa Smolic. Super-resolution of omnidirectional images using adversarial learning. In *2019 IEEE 21st International Workshop on Multimedia Signal Processing (MMSP)*, pages 1–6. IEEE, 2019. [2](#), [3](#), [7](#)
- [32] Yule Sun, Ang Lu, and Lu Yu. Weighted-to-spherically-uniform quality evaluation for omnidirectional video. *IEEE signal processing letters*, 24(9):1408–1412, 2017. [3](#), [6](#), [11](#)
- [33] Yapeng Tian, Yulun Zhang, Yun Fu, and Chenliang Xu. Tdan: Temporally-deformable alignment network for video super-resolution. In *Proceedings of the IEEE/CVF Conference on Computer Vision and Pattern Recognition*, pages 3360–3369, 2020. [4](#)
- [34] Radu Timofte, Eirikur Agustsson, Luc Van Gool, Ming-Hsuan Yang, and Lei Zhang. Ntire 2017 challenge on single image super-resolution: Methods and results. In *Proceedings of the IEEE conference on computer vision and pattern recognition workshops*, pages 114–125, 2017. [5](#)
- [35] Xintao Wang, Kelvin CK Chan, Ke Yu, Chao Dong, and Chen Change Loy. Edvr: Video restoration with enhanced deformable convolutional networks. In *Proceedings of the IEEE/CVF Conference on Computer Vision and Pattern Recognition Workshops*, pages 0–0, 2019. [3](#), [4](#)
- [36] Xintao Wang, Liangbin Xie, Chao Dong, and Ying Shan. Real-esrgan: Training real-world blind super-resolution with pure synthetic data. In *Proceedings of the IEEE/CVF International Conference on Computer Vision*, pages 1905–1914, 2021. [2](#)
- [37] Xintao Wang, Ke Yu, Shixiang Wu, Jinjin Gu, Yihao Liu, Chao Dong, Yu Qiao, and Chen Change Loy. Esrgan: Enhanced super-resolution generative adversarial networks. In *Proceedings of the European conference on computer vision (ECCV) workshops*, pages 0–0, 2018. [2](#), [6](#), [14](#)
- [38] Zhou Wang, Alan C Bovik, Hamid R Sheikh, and Eero P Simoncelli. Image quality assessment: from error visibility to structural similarity. *IEEE transactions on image processing*, 13(4):600–612, 2004. [6](#)
- [39] Zhuofan Xia, Xuran Pan, Shiji Song, Li Erran Li, and Gao Huang. Vision transformer with deformable attention. In *Proceedings of the IEEE/CVF Conference on Computer Vision and Pattern Recognition*, pages 4794–4803, 2022. [3](#)
- [40] Jianxiong Xiao, Krista A Ehinger, Aude Oliva, and Antonio Torralba. Recognizing scene viewpoint using panoramic place representation. In *2012 IEEE Conference on Computer Vision and Pattern Recognition*, pages 2695–2702. IEEE, 2012. [1](#), [6](#)
- [41] Youngho Yoon, Inchul Chung, Lin Wang, and Kuk-Jin Yoon. Spheresr: 360deg image super-resolution with arbitrary projection via continuous spherical image representation. In *Proceedings of the IEEE/CVF Conference on Computer Vision and Pattern Recognition*, pages 5677–5686, 2022. [1](#), [2](#), [7](#), [12](#)
- [42] Kai Zhang, Jingyun Liang, Luc Van Gool, and Radu Timofte. Designing a practical degradation model for deep blind image super-resolution. In *Proceedings of the IEEE/CVF International Conference on Computer Vision*, pages 4791–4800, 2021. [2](#)
- [43] Wenlong Zhang, Yihao Liu, Chao Dong, and Yu Qiao. Ranksgan: Generative adversarial networks with ranker for image super-resolution. In *Proceedings of the IEEE/CVF International Conference on Computer Vision*, pages 3096–3105, 2019. [2](#)
- [44] Yulun Zhang, Kunpeng Li, Kai Li, Lichen Wang, Bineng Zhong, and Yun Fu. Image super-resolution using very deep residual channel attention networks. In *Proceedings of the European conference on computer vision (ECCV)*, pages 286–301, 2018. [1](#), [2](#), [6](#), [7](#), [12](#), [13](#), [14](#)
- [45] Yupeng Zhang, Hengzhi Zhang, Daojing Li, Liyan Liu, Hong Yi, Wei Wang, Hiroshi Saitoh, and Makoto Odamaki. Toward real-world panoramic image enhancement. In *Proceedings of the IEEE/CVF Conference on Computer Vision and Pattern Recognition Workshops*, pages 628–629, 2020. [2](#)
- [46] Yufeng Zhou, Mei Yu, Hualin Ma, Hua Shao, and Gangyi Jiang. Weighted-to-spherically-uniform ssim objective quality evaluation for panoramic video. In *2018 14th IEEE International Conference on Signal Processing (ICSP)*, pages 54–57. IEEE, 2018. [6](#)
- [47] Xizhou Zhu, Han Hu, Stephen Lin, and Jifeng Dai. Deformable convnets v2: More deformable, better results. In *Proceedings of the IEEE/CVF conference on computer vision and pattern recognition*, pages 9308–9316, 2019. [5](#)

Appendix

Due to the lack of space in the main paper, we provide more details of the proposed OSRT in the supplementary file. In Appendix A, we show the transformation relationships from the uniformed sphere to various projection types (ERP, Fisheye, and Perspective) and the derivation processes of each projection type. More experimental details and interpretations can be found in Appendix B. Then we provide additional visual comparisons and visualizations under various projection types in Appendix C.

A. Geometric Relationship

In this section, x_E, y_E and x_P, y_P refer to plane coordinates of ERP and Perspective, respectively. For an ideal sphere, θ_S, φ_S are the spherical coordinates, and x_S, y_S, z_S are the space coordinates. ρ_F, θ_F and x_F, y_F are polar coordinates and plane coordinates of Fisheye, respectively.

A.1. Transformation

ERP. For ERP, the coordinate is defined as:

$$\begin{cases} x_E = \theta_S \\ y_E = \varphi_S. \end{cases} \quad (10)$$

Fisheye. For Fisheye, the coordinate is defined as:

$$\begin{cases} \rho_F = 2 \times \arctan(\sqrt{x_S^2 + y_S^2/z_S^2})/A_F \\ \theta_F = \arctan(y_S/x_S) \\ x_S = \rho_F \times \cos(\theta_F) \\ y_S = \rho_F \times \sin(\theta_F), \end{cases} \quad (11)$$

where A_F is the aperture degree of Fisheye. Specifically, when the normal vector of the Fisheye splicing plane is parallel to the z-axis, Eq. (11) can be simplified as:

$$\begin{cases} \rho_F = 2 \times (\pi/2 - \varphi_S)/A_F \\ \theta_F = \theta_S. \end{cases} \quad (12)$$

Here, we define a rotation transformation under the spherical coordinates:

$$[x_S^*, y_S^*, z_S^*]^T = M_r \cdot [x_S, y_S, z_S]^T, \quad (13)$$

where M_r is the 3D rotation matrix. $[x_S, y_S, z_S]^T$ and $[x_S^*, y_S^*, z_S^*]^T$ are the original and rotated spherical coordinates, respectively. Eq. (13) is defined to align general Fisheye to the horizontally spliced one, which is identical to add $\Delta\theta_r, \Delta\varphi_r$ on spherical polar coordinates.

Perspective. The coordinates is defined as:

$$\begin{cases} x_P = \tan(\theta_S) \\ y_P = \tan(\varphi_S)/\cos(\theta_S), \end{cases} \quad (14)$$

where $x_P, y_P \in [-\tan(A_P/2), \tan(A_P/2)]$. A_P is the aperture degree of Perspective, which determines the field-of-view (FOV) of the given Perspective. Note that a perspective image only represents information on a partial area of a spherical surface.

A.2. Distortion

As mentioned in the main paper, the distortion degree of each projection type is measured by [32]:

$$\mathbf{K}(x, y) = \frac{\delta S(\theta, \varphi)}{\delta P(x, y)} = \frac{\cos(\varphi)|d\theta d\varphi|}{|dxdy|} = \frac{\cos(\varphi)}{|J(\theta, \varphi)|}, \quad (15)$$

where $\delta S(\cdot, \cdot)$ and $\delta P(\cdot, \cdot)$ represent the area on the spherical surface and the projection plane, respectively. $|didj|$ represents a plane microunit. $|J(\theta, \varphi)|$ is the Jacobian determinant from spherical coordinate to projection coordinate.

ERP distortion. From Eqs. (10) and (15), ERP stretching ratio can be derived as:

$$\mathbf{K}_{\text{ERP}}(x_E, y_E) = \cos(\varphi_S) = \cos(y_E). \quad (16)$$

Fisheye distortion. In this paragraph, we denote A_F as π . $|J_F^*(\theta_S, \varphi_S)|$ can be simplified by Eq. (12):

$$\begin{aligned} & |J_F^*(\theta_S, \varphi_S)| \\ &= \begin{vmatrix} \frac{\partial(x_F)}{\partial(\theta_S)} & \frac{\partial(x_F)}{\partial(\varphi_S)} \\ \frac{\partial(y_F)}{\partial(\theta_S)} & \frac{\partial(y_F)}{\partial(\varphi_S)} \end{vmatrix} \\ &= \begin{vmatrix} \frac{\partial(\rho_F \cos \theta_F)}{\partial(\theta_S)} & \frac{\partial(\rho_F \cos \theta_F)}{\partial(\varphi_S)} \\ \frac{\partial(\rho_F \sin \theta_F)}{\partial(\theta_S)} & \frac{\partial(\rho_F \sin \theta_F)}{\partial(\varphi_S)} \end{vmatrix} \\ &= \begin{vmatrix} \frac{\partial((1-2\varphi_S/\pi) \cos \theta_S)}{\partial(\theta_S)} & \frac{\partial((1-2\varphi_S/\pi) \cos \theta_S)}{\partial(\varphi_S)} \\ \frac{\partial((1-2\varphi_S/\pi) \sin \theta_S)}{\partial(\theta_S)} & \frac{\partial((1-2\varphi_S/\pi) \sin \theta_S)}{\partial(\varphi_S)} \end{vmatrix} \\ &= \begin{vmatrix} -(1-2\varphi_S/\pi) \sin \theta_S & -2 \cos \theta_S/\pi \\ (1-2\varphi_S/\pi) \cos \theta_S & -2 \sin \theta_S/\pi \end{vmatrix} \\ &= \frac{2}{\pi} (1-2\varphi_S/\pi) (\sin^2 \theta_S + \cos^2 \theta_S) \\ &= \frac{2}{\pi} \rho_F. \end{aligned} \quad (17)$$

From Eqs. (12), (15) and (17), the stretching ratio of horizontally spliced Fisheye can be derived as:

$$\begin{aligned} \mathbf{K}_{\text{Fisheye}}^*(x_F, y_F) &= \frac{\cos(\varphi_S)}{|J_F(\theta_S, \varphi_S)|} \\ &= \frac{\cos(\frac{\pi}{2}(1-\rho_F))}{\frac{2}{\pi} \rho_F}. \end{aligned} \quad (18)$$

Then, we can derive stretching ratio of general Fisheye

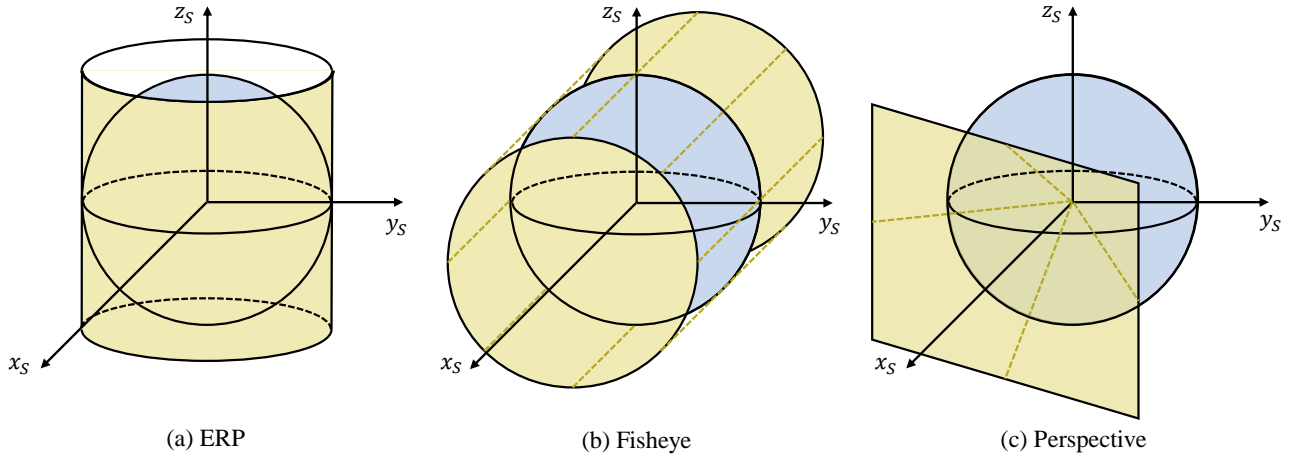


Figure 10. Geometric illustration of three projection types. Blue and yellow refer to the spherical surface and projection plane, respectively.

from Eqs. (15), (17) and (18):

$$\begin{aligned}
 \mathbf{K}_{\text{Fisheye}}(x_F, y_F) &= \frac{\delta S(\theta_S, \varphi_S)}{\delta P(x_F, y_F)} \\
 &= \underbrace{\frac{\delta S(\theta_S^*, \varphi_S^*)}{\delta P(x_F, y_F)}}_{\text{Projection}} \cdot \underbrace{\frac{\delta S(\theta_S, \varphi_S)}{\delta S(\theta_S^*, \varphi_S^*)}}_{\text{Rotation}} \\
 &= \mathbf{K}^* \cdot \frac{\cos(\varphi_S) |d\theta_S d\varphi_S|}{\cos(\varphi_S^*) |d\theta_S^* d\varphi_S^*|} \\
 &= \mathbf{K}^* \cdot \frac{\cos(\varphi_S^* + \Delta\varphi_r)}{\cos(\varphi_S^*)} \\
 &= \frac{\cos(\frac{\pi}{2}(1 - \rho_F) - \Delta\varphi_r)}{\frac{2}{\pi}\rho_F},
 \end{aligned} \tag{19}$$

where $\Delta\varphi_r$ is a constant, which is determined by the angle between the normal vector of splicing plane and z-axis.

Perspective. From Eqs. (14) and (15), the Perspective stretching ratio can be derived as:

$$\begin{aligned}
 \mathbf{K}_{\text{Perspective}}(x_P, y_P) &= \frac{\cos(\varphi_S)}{|J_P(\theta_S, \varphi_S)|} \\
 &= \cos^3(\theta_S) \cos^3(\varphi_S) \\
 &= (1 + x_P^2 + y_P^2)^{-\frac{3}{2}}.
 \end{aligned} \tag{20}$$

	Original	Cleaned
Num of images in ODI-SR (training)	1200	1150
Num of images in ODI-SR (testing)	100	100
Num of images in ODI-SR (validation)	100	97
Num of images in SUN360	100	100
Downsampling function	OpenCV	Pillow
Downsampling target	ERP	Dual Fisheye
Storage format	JPEG	PNG

Table 5. Differences between the original and cleaned datasets.

B. Details and Discussions

B.1. Data Cleaning on ODI Dataset

Except for ERP downsampling, we still find other issues in both ODI-SR and SUN360 datasets. Previous datasets are downsampled by bicubic function without anti-alias design (OpenCV-Python), which introduces mottled artifacts (Fig. 11). Meanwhile, they are stored in the format of JPEG, which leads to missing details and JPEG-blocking artifacts. Storing HR images in JPEG format is harmful for both training and evaluation. To tackle these issues, we propose to apply downsampling by anti-aliased bicubic function (Pillow) and store images in a lossless format (PNG). Moreover, there are problematic ODIs in previous datasets: **1)** transforming mistakes; **2)** virtual scenarios; **3)** extremely low qualities; **4)** plane images. Consequently, we propose ODI-SR-clean and SUN360-clean datasets, the differences are shown in Tab. 5. We train and test all models on cleaned datasets except the comparison under ERP downsampling (Sec. 4.3 in the main paper).

When comparing SR results under ERP downsampling, we train and test models on original datasets, which is identical to previous methods. Thus we can directly compare the SR results of OSRT with SR results reported by previous methods, *e.g.*, LAU-Net [13] and SphereSR [41].

B.2. Instability of RCAN

For RCAN [44] trained with Fisheye downsampling, the training process is unstable and thus the performance is degraded. We find that the instability of RCAN is caused by incompatibility between the channel attention block (CAB) and Fisheye downsampling. CAB requires global statistical features, and its training stability depends on the consistent mean value distribution of each patch [10]. However, when Fisheye downsampling is applied to an ERP image, the ERP image suffers from nonuniform downsampling, which di-

Backbone network	Datasets	Training scheme	Scale	ODI-SR		SUN360	
				PSNR	SSIM	PSNR	SSIM
SwinIR	ODI-SR	N/A		30.52	0.8819	31.21	0.8852
SwinIR	DF2K/ODI-SR	one-stage	×2	30.59	0.8810	31.26	0.8841
SwinIR	DF2K-ERP/ODI-SR	one-stage		30.64	0.8821	31.33	0.8855
SwinIR	DF2K-ERP/ODI-SR	two-stage		30.54	0.8797	31.17	0.8818
OSRT	DF2K-ERP/ODI-SR	one-stage		30.77	0.8846	31.52	0.8888
SwinIR	ODI-SR	N/A		27.12	0.7663	27.39	0.7707
SwinIR	DF2K/ODI-SR	one-stage	×4	27.24	0.7708	27.59	0.7768
SwinIR	DF2K-ERP/ODI-SR	one-stage		27.31	0.7735	27.71	0.7804
SwinIR	DF2K-ERP/ODI-SR	two-stage		27.33	0.7725	27.74	0.7795
OSRT	DF2K-ERP/ODI-SR	one-stage		27.41	0.7762	27.84	0.7835

Table 6. Ablation study on data augmentation.

Method	Scale	ODI-SR		SUN 360 Panorama	
		PSNR	SSIM	PSNR	SSIM
RCAN [44]	×2	30.08	0.8723	30.56	0.8712
RCAN-local [10]		30.28	0.8735	30.80	0.8740
RCAN [44]	×4	26.85	0.7621	27.10	0.7660
RCAN-local [10]		26.99	0.7622	27.24	0.7665

Table 7. Influence of test-time local converter.

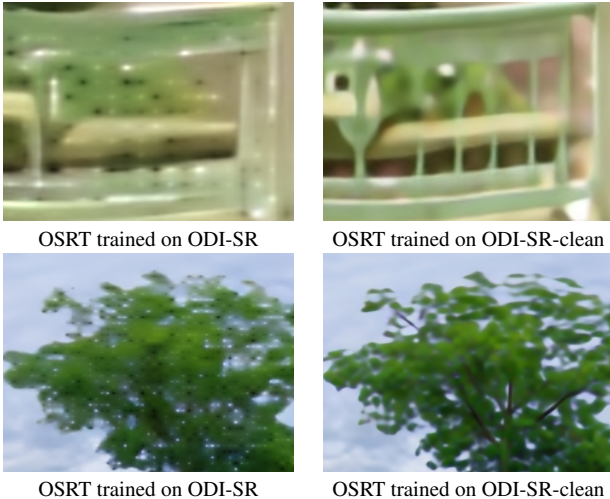


Figure 11. Visual comparisons of ×8 SR results trained and tested on the original and cleaned datasets.

rectly increases the mean value diversity between patches. Although implementing a test-time local converter (TLC [10]) can reduce the distribution gap between the patch and the whole image (Tab. 7), it cannot reduce the distribution gap within patches. Consequently, while training ODISR models under Fisheye downsampling, blocks that require global statistical values are not recommended.

B.3. Full Ablation Results of Data Augmentation

Due to the lack of space in the main paper, we only show partial ablation results of data augmentation strategies (Tab. 4). The full results are shown in Tab. 6. Compared with fine-tuning on DF2K-ERP pre-trained models (two-stage), training on two datasets jointly (one-stage) shows better re-

sults. Moreover, the advantage of OSRT is enlarged when additional training patches are applied.

B.4. Domain Gap between Real and Pseudo ODIs

As mentioned in the main paper (Sec. 3.4), we synthesize pseudo ERP training data (DF2K-ERP) from the plain images to alleviate the over-fitting problem of large networks. Although DF2K-ERP has shown obvious benefits, there is still a domain gap between real and pseudo images. From Eq. (20), we can see that the distortion degree of Perspective is determined by the distance from the center. As the projection range is determined by FOV degree, perspective images with different FOV degrees suffer inconsistent distortions. However, we cannot obtain the distribution of FOV degrees in real-world scenarios. Thus we directly assume that all pseudo perspective images have a fixed FOV degree of 90°, which introduces a domain gap. While the inevitably domain gap is a limitation of DF2K-ERP, it still overcomes the over-fitting issue and improves the reconstruction ability.

C. Visualization

As mentioned in the main paper (Sec. 3.2), ERP downsampling leads to unrealistic ODIs. Thus we only show visualizations based on Fisheye downsampling in this section.

Additional qualitative comparison. We provide additional visual comparisons with other methods on the ODI-SR-clean testing dataset and SUN360-clean dataset in Fig. 12. Reconstructed ERP images are compared under ERP, Fisheye, and Perspective. As shown in Fig. 12 (d) and (f), we can see that OSRT can reconstruct sharp and accurate boundaries. Besides, from Fig. 12 (a) and (c), we conclude that OSRT is skilled at reconstructing rigid textures.

Additional visualization of OSRT. To show the overall quality of OSRT reconstructed images, we project these ERP images to arbitrary projection types. Figs. 13 to 15 depict visualizations of ×2, ×4 and ×8 SR results, respectively. Under all projection types, OSRT can reconstruct details with high fidelity (buildings in Fig. 13, tiles in Fig. 14, and grasses in Fig. 15).

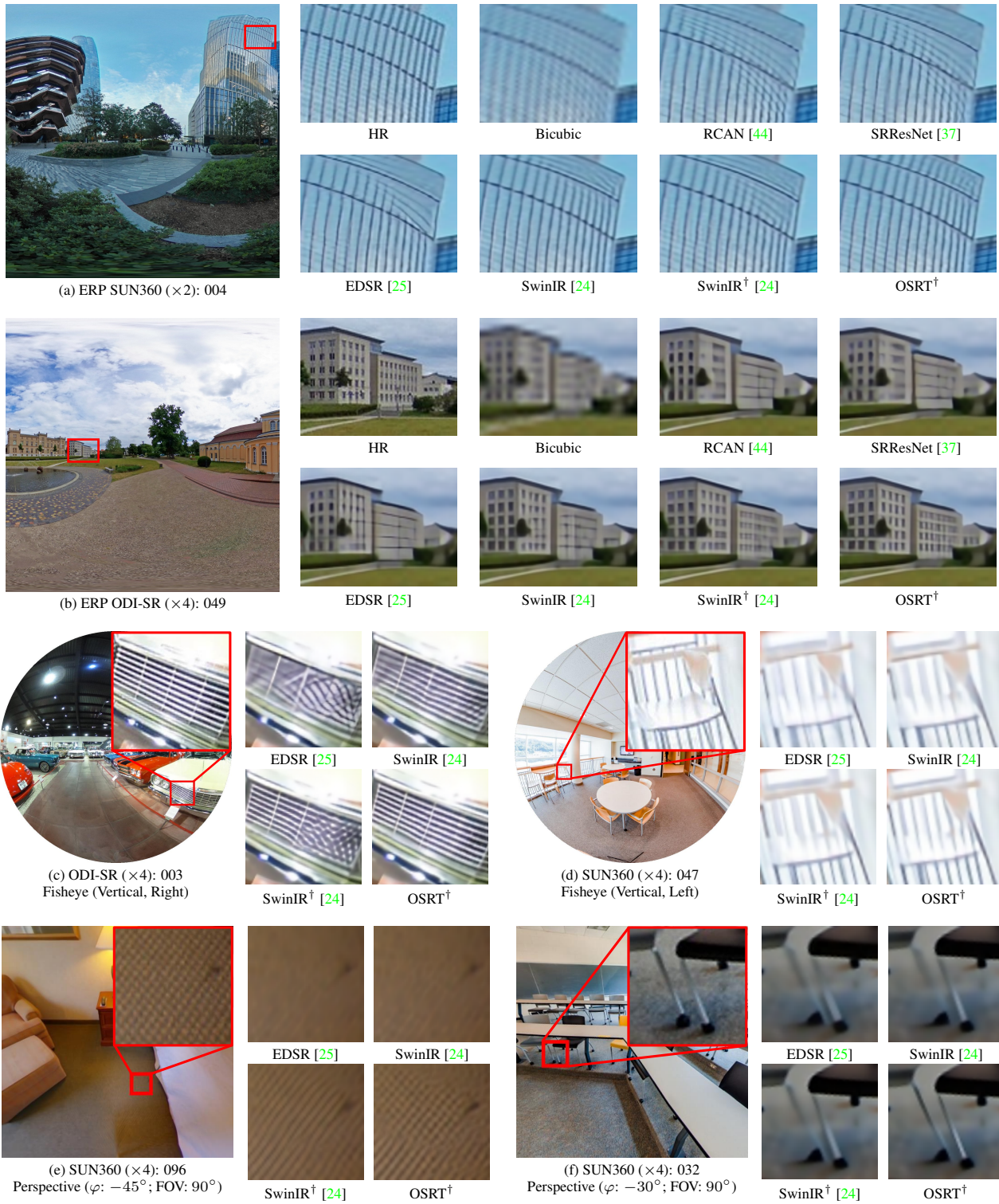
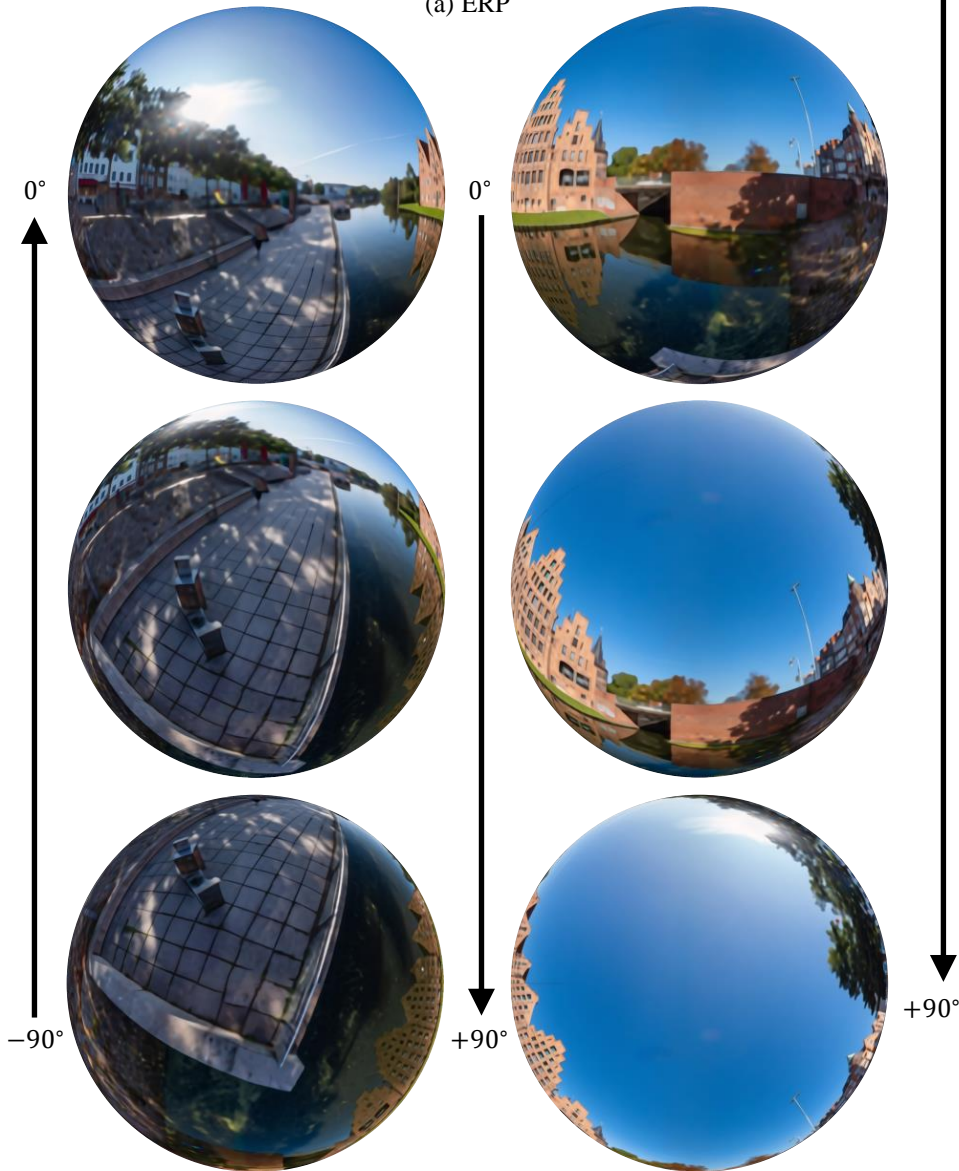


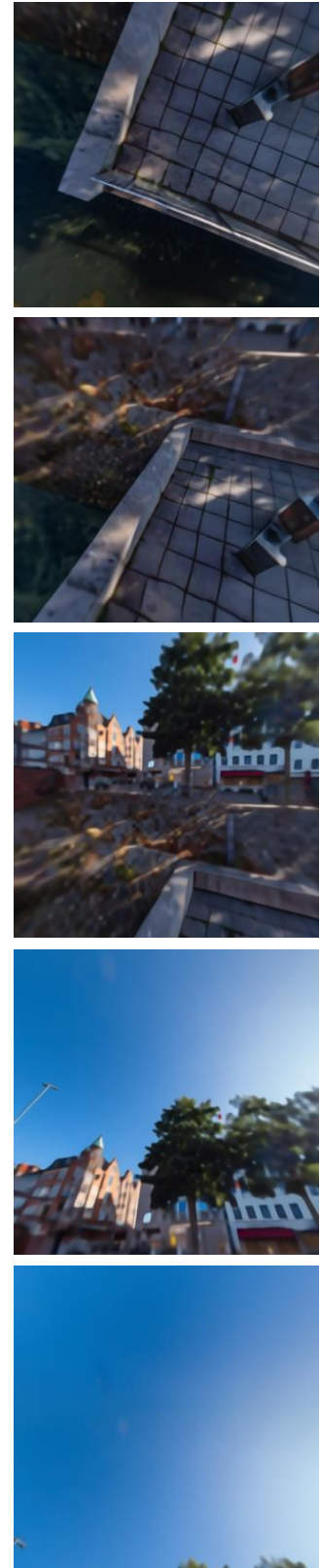
Figure 12. Visual comparisons of SR results under Fishey downsampling. † denotes applying DF2K-ERP as augmented dataset.



(a) ERP



(b) Fisheye



(c) Perspective

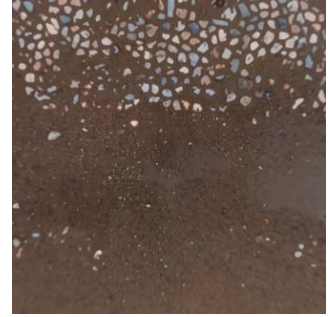
Figure 13. Visualization of $\times 8$ SR results (SUN360-062).



(a) ERP



(b) Fisheye

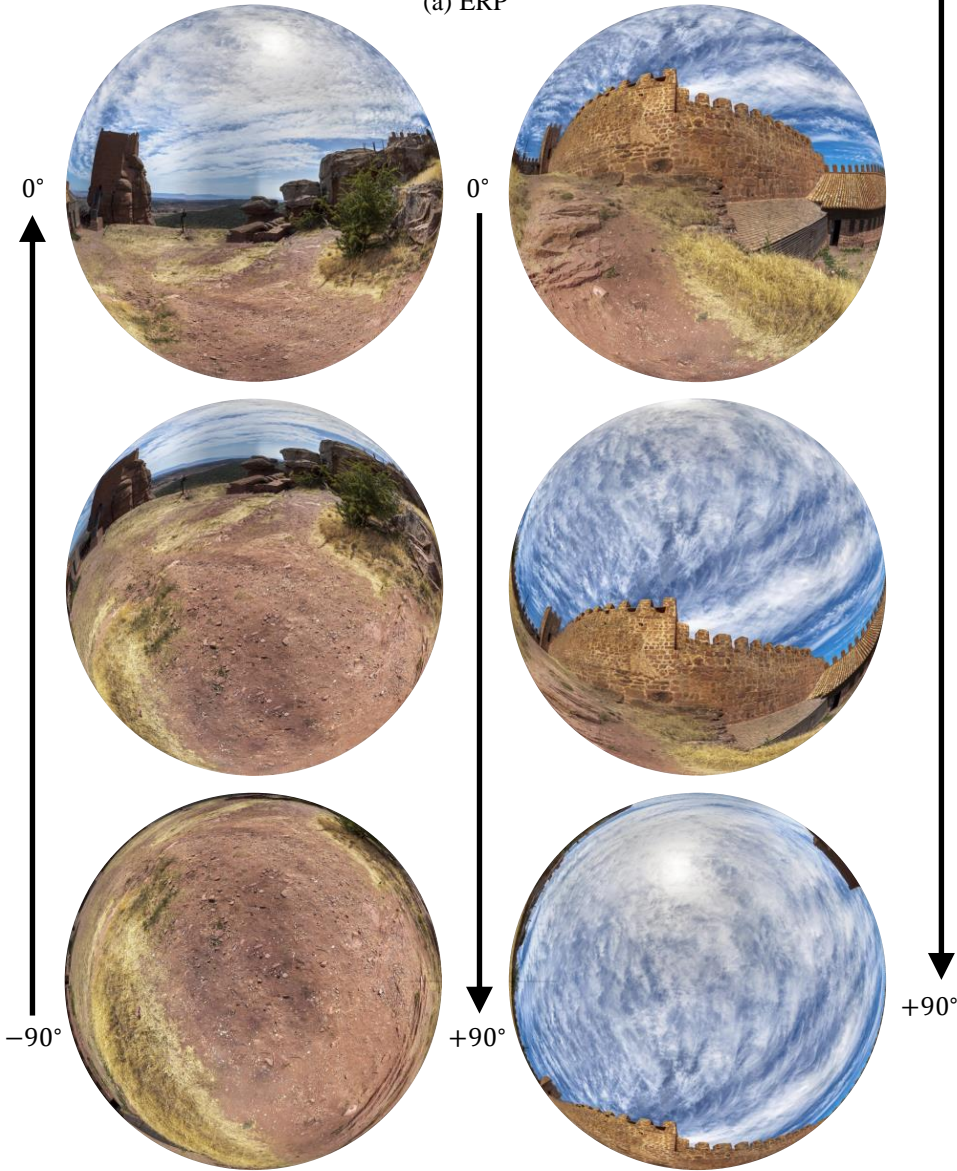


(c) Perspective

Figure 14. Visualization of $\times 4$ SR results (ODI-SR-066).



(a) ERP



(b) Fisheye



(c) Perspective

Figure 15. Visualization of $\times 2$ SR results (SUN360-007).